PAPER

Check for updates

Pressure-promoted highly-ordered Fe-doped-Ni₂B for effective oxygen evolution reaction and overall water splitting†

HPSTAR
1275-2021

Ruifeng Tian,‡[a] Shijing Zhao,‡[b] Junkai Li,‡[b] Zhibin Chen,[a] Wenfeng Peng, [b] Yan He,[c] Lili Zhang,[c] Shuai Yan,[c] Lailei Wu, *[a] Rajeev Ahuja [d] and Huiyang Gou *[b]

Accurate doping at special atomic sites can achieve effective control of active centers for the oxygen evolution reaction (OER), leading to the synthesis of active intermediates with higher conversion efficiency. Here we report the successful doping of Ni₂B with Fe/Co to form highly ordered FeNiB and CoNiB electrocatalysts with a tetragonal Ni₂B structure. A highly crystalline FeNiB electrode is found to have a very low polarization overpotential of 257 mV for the OER and a water splitting potential of 1.54 V at a current density of 10 mA cm⁻². XRD refinement, XPS and XAFS characterization found that doping with iron leads to the weakening of the bond strength of TM−B, which facilitates the adsorption of oxygen. During the OER process, the increasing dissolution of boron oxides promotes the effective exposure of metal active centers and boosts the catalytic performance. Theoretical calculations reveal that the substitution of Fe atoms in Ni₂B make its DOS near the Fermi level higher by 2.78 times compared to that of the original Ni₂B, which helps to increase the electronic conductivity and the catalytic performance.

Introduction

The conversion and storage of intermittent energy is a promising strategy to satisfy the increasing demand for energy. This objective may be achieved by electrochemical splitting of water to produce hydrogen.[1] Water splitting consists of a cathodic process producing H_2 and an anodic process producing O_2. The mechanism of the hydrogen evolution reaction (HER) is relatively clear and a great number of high-performance catalysts have been developed to generate hydrogen at a fairly low polarization potential. While the anodic process (the oxygen evolution reaction, OER) is a thermodynamically uphill reaction of water electrolysis, which involves transfer of four electrons and splitting of two water molecules, relatively high activation energy is required to break the O–H bonds and form O–O bonds at the same time.[2] Noble metal-based catalysts (RuO_2 and IrO_2)

State Key Laboratory of Metastable Materials Science and Technology, College of Material Science and Engineering, Yanshan University, Qinhuangdao 066004, China. E-mail: wll@ysu.edu.cn

Center for High Pressure Science and Technology Advanced Research, Beijing 100094, China. E-mail: huiyang.gou@hpstar.ac.cn

Shanghai Synchrotron Radiation Facility, Shanghai Advanced Research Institute, Chinese Academy of Sciences, Shanghai 201203, China

Condensed Matter Theory Group, Department of Physics & Astronomy, Uppsala University, 751 20 Uppsala, Sweden

† Electronic supplementary information (ESI) available. See DOI: 10.1039/d0ta10010b

‡ RT, SZ and JL contributed equally to this work.

are able to substantially reduce the reaction activation energy for the OER and are widely used for commercial production.[3] However, their high cost and rarity pose great challenges for their wide industrial application. Therefore, the development of low-cost and highly efficient electrocatalysts for the OER is imperative. In the few past decades, non-noble transition metal oxides,[4–6] phosphides,[7–9] sulfides[10–12] and nitrides[13] have been explored as potential candidates for the HER and OER. In particular, transition metal borides (TMBs) with good conductivity, low cost, environmental benignity and abundant resources have been suggested as potential candidates for use as OER catalysts. Hitherto, most TMBs have been synthesized using conventional solution chemistry methods,[14,15] which usually lead to the presence of an amorphous structure. Crystallized TMBs, as traditional high hardness, corrosion-proof, and magnetic materials, attract less interest for electrocatalysis.[16–18] Due to the inherent inertia of boron, the reaction energy barrier is high between boron and metal atoms, which limits the exploration of crystalline TMBs as catalysts. A high pressure and high temperature (HPHT) methodology, different from conventional synthesis methods, is found to be a feasible tool to synthesize borides, for example, boron-rich compounds, $Mo_{0.757}B_3$ and FeB_4.[19,20] Crystalline borides provide an opportunity to study the intrinsic properties of electro-catalysts. The stoichiometric ratio of metal atoms can be precisely controlled by HPHT to optimize the surface adsorption energy of the material and make it closer to the peak of the adsorption energy volcano.

This journal is © The Royal Society of Chemistry 2021

J. Mater. Chem. A, 2021, **9**, 6469–6475 | **6469**

In this work, we synthesized highly crystalline transition metal borides (Fe, Co doped Ni_2B; TM_2B, TM = Fe/Co and Ni) *via* the HPHT method to explore the intrinsic catalytic properties of bimetallic boride materials. Our results reveal that FeNiB exhibits an overpotential of 257 mV for the OER, which achieves the best performance among all three samples, much better than that of commercial benchmark RuO_2 and some amorphous transition metal borides.[14,15,21] FeNiB also exhibits an excellent stability for the OER process. After 30 hours of electrochemical testing, the degree of polarization increased by only 7%. Meanwhile, FeNiB exhibits prominent overall water splitting properties with a potential of 1.54 V, and outperforms most of the available boride catalysts. Furthermore, the first-principles calculations are also performed to explain the outstanding performance of FeNiB. Through the analysis of TEM, XPS and XAS and the electronic structure, the underlying mechanism of the outstanding OER performance of FeNiB is understood.

Results and discussion

Ni_2B and Fe/Ni doped Ni_2B were synthesized under 5 GPa and at 1300 °C (further details can be found in the experimental method section in the ESI†). As shown in Fig. 1a, all the samples show single phase characters with a highly crystalline tetragonal Ni_2B structure (space group: *I4/mcm*, PDF no. 48-1222). In comparison with Ni_2B, the diffraction peaks of FeNiB and CoNiB slightly shift to a lower angle, due to the relatively larger atomic radii of Fe/Co than Ni. Rietveld refinements (Fig. S2†) are also performed to obtain detailed information about the cell parameters and bond lengths. The *a/c* value of the three samples shown in Table S1† almost increase linearly with the

increased radii of the doping elements while the *c* direction of CoNiB and FeNiB is found to be almost squeezed when doped with cobalt and iron elements with larger radii. The distance of B–B bonds is approximately 2.1 Å (Table S2†), longer than the sum of the covalent radius of boron (0.85 Å), indicating a relatively weak interaction between boron atoms. The greater bond lengths of TM–B in FeNiB suggest that the bond strengths between B and Fe are not as strong as the bond strength between B and Ni/Co in Ni_2B/CoNiB as shown in Fig. 1b. Scanning electron microscopy (SEM) images after ball-milling for 10 h at 350 rpm are shown in (Fig. S3a–c†). Energy dispersive spectroscopy (EDS) mapping (Fig. S3d and e†) shows a highly homogeneous distribution of Fe and Ni elements; the stoichiometric ratio between Fe/Co and Ni is very close to 1 : 1 for FeNiB/CoNiB as shown by quantitative analysis (Fig. S4–S6†). In order to obtain more detailed information about the micro-structure of tetragonal TM_2B borides, FeNiB is selected to be characterized using a transmission electron microscope (TEM) and high-resolution transmission electron microscope (HRTEM) (Fig. 1c–e). The HRTEM image (Fig. 1e) and selected area electron diffraction (SAED, Fig. 1e inset) pattern of FeNiB reflect the highly ordered single-crystalline structure. In the HRTEM image, the lattice fringe of 0.2497 nm corresponds to the (200) crystal planes of Ni_2B (0.2495 nm); a slight difference arises from the introduction of Fe atoms. EDS mapping (Fig. 1f) shows a highly homogeneous distribution of elements, consistent with SEM and TEM results.

The electrocatalytic performance of all three TMNiB samples is tested with a standard three electrode system in 1 M KOH solution in comparison with that of commercial RuO_2. Fig. 2a shows the linear sweep voltammetry (LSV) results of OER performance. As we can see, FeNiB exhibits the best OER performance with a quite low overpotential of 257 mV at current density of 10 mA cm^{-2} (η_{10}), and outperforms the previously reported transition metal borides.[22–28] Nevertheless, both CoNiB (η_{10} = 302 mV) and Ni_2B (η_{10} = 300 mV) are inferior to RuO_2 (η_{10} = 284 mV) at current densities lower than 30 mA cm^{-2}. FeNiB also exhibits the lowest Tafel slope of 110 mF dec^{-1} (Fig. 2b), which indicates the most feasible OER reactive nature of FeNiB. The electrochemical surface area (ECSA) of all samples is estimated from their surface specific double layer capacitance (C_{dl}). C_{dl} is obtained by cyclic voltammetry (CV) at different scan rates (20–100 mV s^{-1}) in a non-faradaic region (0.1–0.2 V *vs.* Hg/HgO), and a general specific capacitance of 0.04 mF cm^{-2} in 1.0 M alkaline media is adopted for metal electrodes as reported in many previous reports.[29] Fig. S7† shows the CV curves for ECSA calculations and Fig. 2c shows the calculated C_{dl} of all four samples. The difference of the ECSA is mainly caused by the adsorption capacity of Ni/Co/Fe on OH$^-$ from the electrolyte because the three synthesized samples have almost the same specific surface area, which can be reflected by the same crystal structure and similar particle size/morphology shown in Fig. S3.† When nickel is substituted by cobalt in CoNiB, C_{dl} increases by about 70%, but the ECSA has no significant changes. However, when nickel is substituted by iron, a remarkable increase of the ECSA is found whereas C_{dl} decreases by about 10%. The ECSA results indicate that Co has
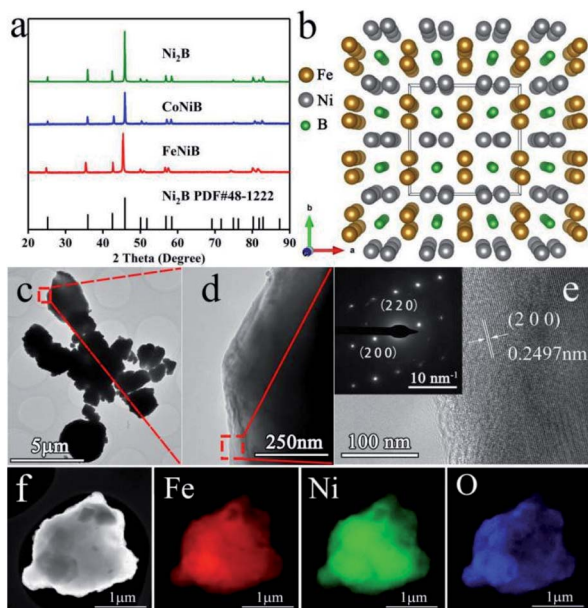
Fig. 1 (a) XRD patterns of Ni_2B, CoNiB and FeNiB. (b) 3D crystal structure of FeNiB. (c and d) TEM images of FeNiB. (e) HRTEM image of FeNiB and the SAED image (inset). (f) EDS mapping of FeNiB.

6470 | *J. Mater. Chem. A*, 2021, **9**, 6469–6475

This journal is © The Royal Society of Chemistry 2021
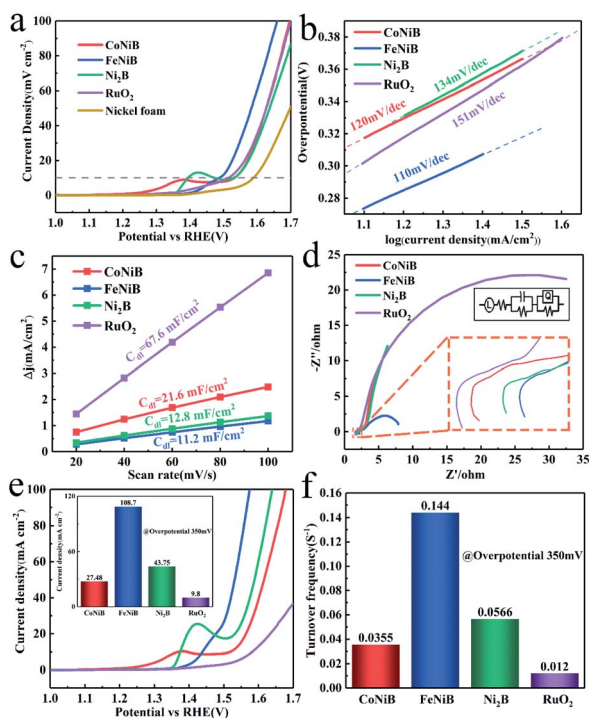
Fig. 2 Electrocatalytic characterization for the OER. (a) LSV curves of the OER obtained at a scan rate of 5 mV s^{-1}. (b) Tafel plots. (c) Electrochemical surface area (ECSA) of CoNiB, FeNiB, Ni$_2$B and RuO$_2$. (d) Nyquist plots, with the inset showing the equivalent circuit. (e) LSV curve modified by the ECSA and current density at 350 mV overpotential. (f) Calculated turnover frequency (TOF) values of all four samples.

Fig. 3 (a) Overall water splitting curves with the overpotential at 10 mA cm^{-2} current density. (b) Summary of the overpotential and overall water splitting performance of metal borides in different studies. (c) Chronoamperometry curve of FeNiB obtained at 100 mA cm^{-2}. (d) LSV curves of initial and after 10 000 cycles of FeNiB.

the highest efficiency of adsorption and desorption for hydroxyl but there is no evident improvement in OER properties, and Fe possesses the best binding effect towards the OER reactant (OH$^-$). It can thus be concluded that the ECSA is not the critical factor for the catalytic properties, and Fe is suggested to be the active site and responsible for the enhanced OER properties in such an alkaline environment. Fig. 2e shows the ECSA modified LSV curves for OER performance. All three borides exhibit much better OER performance compared to RuO$_2$, due to the relatively low ECSA. The current density of FeNiB at an overpotential of 350 mV is 108.7 mA cm^{-2}, which is 11 times higher than that of RuO$_2$ (9.8 mA cm^{-2}), 4 times higher than that of CoNiB (27.48 mA cm^{-2}) and 2.5 times higher than that of Ni$_2$B (43.75 mA cm^{-2}). Generally, the best performance could also belong to the one with the highest ECSA.[30–32] And LSV curves normalized by the specific surface area also present similar results shown in Fig. S8b.† However, FeNiB obtained the lowest C_{dl} (11.2 mF cm^{-2}) among all four samples but showed the best performance, which can be attributed to the highest turnover frequency (TOF) of the active sites. For heterogeneous catalysis, the active sites can be a low coordination terrace, kink, edge and corner.[33] In this regard, the different types of active sites lead to different catalytic activities. As shown in Fig. 2f, FeNiB achieves a very high TOF value of 0.144 s^{-1}, which is 11.8 times higher than that of RuO$_2$ (0.0120 s^{-1}), 4.05 times higher than that of CoNiB (0.0355 s^{-1}) and 2.54 times higher than that of Ni$_2$B

(0.0566 s^{-1}). The high TOF value indicates a high catalytic performance per active site, which is an intrinsic property of electrocatalysts. Furthermore, the electrical conductivity of catalysts is measured by electrochemical impedance spectroscopy (EIS). As shown in Fig. 2d and Table S3,† all four samples obtain a solution resistance (R_{sol}) around 2 Ω, with the sequence of RuO$_2$ < CoNiB < Ni$_2$B < FeNiB. However, the charge transfer resistance of electrocatalysts (R_{ct}) of FeNiB (3.335 Ω) is significantly lower than that of the other samples (RuO$_2$: 42.05 Ω; CoNiB: 43.75 Ω; Ni$_2$B: 67.94 Ω), indicating an outstanding electroconductivity of FeNiB. Overall water splitting is also tested using nickel foam loaded samples as the anode and Pt foil as the cathode. The overall water splitting curves of all samples and pure nickel foam are shown in Fig. 3a. FeNiB also exhibits the best performance of water splitting with a potential of 1.54 V at 10 mA cm^{-2} current density. This is an excellent value among metal boride catalysts. The overall water splitting potentials at a current density of 10 mA cm^{-2} of CoNiB, Ni$_2$B and commercial RuO$_2$ are all above 1.6 V (Fig. 3a), and bare nickel foam shows a scarce activity of 1.68 V.

The overpotentials for the OER and the overall water splitting of all available borides to the best our knowledge are summarized in Tables S4, S5† and Fig. 3b. FeNiB stands out with the lowest overpotential for both the OER and overall water splitting. A long-term stability test is performed via both chronoamperometry and CV methods. Fig. 3c shows the chronoamperometry curve obtained at 100 mA cm^{-2} current density. After a 30-h test, the potential increases by only 7% for FeNiB, indicating great long-term stability. The initial and 10 000 cycled LSV curves for FeNiB are shown in Fig. 3d. Only slight loss of the catalytic activity of FeNiB can be observed compared that of with RuO$_2$ (Fig. S9†).

The surface structure and chemical state are very important for understanding the excellent electrochemical performance. X-ray photoelectron spectroscopy (XPS) is thus performed to evaluate the chemical surface states before and after electrochemical OER tests. The XPS analysis (Fig. S10†) verifies the
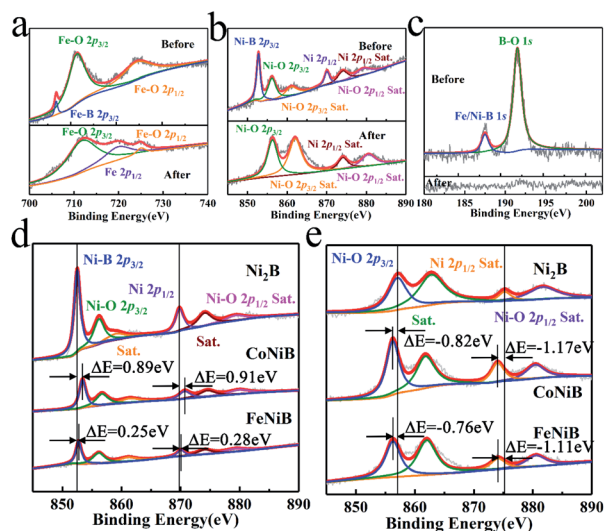
Fig. 4 XPS results of FeNiB (a) Fe 2p, (b) Ni 2p, (c) B 1s before and after the durability test, (d and e) the comparison of Ni 2p results of Ni$_2$B, CoNiB and FeNiB before and after the durability test respectively.

existence of Fe, Ni, B and O elements for FeNiB; Co, Ni, B and O elements for CoNiB and Ni, B and O elements for Ni$_2$B, in good agreement with the SEM and TEM results. The F element is observed after the durability test from the binder PTFE during electrode preparation. For the high resolution spectrum of FeNiB, in Fig. 4a, the peak located at 706.84 eV is indexed to the Fe–B bond, indicating the presence of the TM$_2$B core. The peaks located at 711.33 eV and 724.44 eV are ascribed to Fe–O 2p$_{3/2}$ and Fe 2p$_{1/2}$, explaining the emergence of Fe$_2$O$_3$ or FeOOH.[34] But after the OER test, there exists three different peaks; the peaks at 711.77 eV and 724.99 eV are assigned to Fe–O, which could be FeOOH. In Fig. 4b, the peaks located at 852.77 eV and 870.07 eV are assigned to Ni–B bonds, which disappear after the oxidation reaction. Two peaks at 856.19 eV and 874.08 eV correspond to Ni–O 2p$_{3/2}$ and Ni 2p$_{1/2}$ respectively, revealing the existence of Ni (OH)$_2$ or NiO. However, the peaks of Ni 2p shift to a higher energy at 856.29 eV and 874.10 eV after reaction, which indicates the transformation of Ni (OH)$_2$ to NiOOH. As shown in Fig. 4c, moreover, the peaks of the B1s spectrum at 188.15 eV and 192.00 eV are assigned to the Ni–B/Fe–B bond and boron-oxo species, but after reaction, the Ni–B bond disappears; this scenario may indicate the precipitation of lattice boron and the formation of TM–O bonds on the surface, which is in agreement with Fe 2p spectra. The high resolution XPS spectra of CoNiB and Ni$_2$B (Fig. S11 and S12†) also exhibit the same reconstruction of metal boride to metal oxide transition on the surface after OER tests. Differently, the B–O peak could still be detected in the high-resolution B 1s spectrum of both CoNiB and Ni$_2$B after the OER test, which disappears in FeNiB. Almost all B atoms on the surface of FeNiB participated in the reconstruction reaction after the durability test, owing to the introduction of Fe elements that promotes the dissolution of surface boron atoms.[35]

To further understand the effect of the replacement of Ni atoms by Fe or Co in the Ni$_2$B structure, the Ni 2p spectra of Ni$_2$B, CoNiB and FeNiB are displayed in Fig. 4d with six similar peaks of Ni–B, Ni–O. However, Ni–B (Ni 2p$_{3/2}$) peaks (about 852 eV) of CoNiB and FeNiB shift to a higher binding energy by about 0.89 eV and 0.25 eV, and Ni–B (Ni 2p$_{1/2}$) peaks shift by 0.91 eV and 0.28 eV for CoNiB and FeNiB, respectively. On the one hand, the electrons transfer between Fe and B atoms is more easily than that between Co and B atoms because of the difference of electronegativity between metal and boron. So, the change of the binding energy of nickel in FeNiB is relatively smaller than that of nickel in CoNiB. On the other hand, the bond lengths of TM–B (2.140 Å) in Ni$_2$B are much shorter than those of CoNiB (2.160 Å) and FeNiB (2.162 Å). Therefore, the stronger covalent Ni–B bonds make the nickel atoms keep the lower binding energy. The longer bond lengths of TM–B in CoNiB and FeNiB may provide more space for absorbing oxygen, promoting the OER. In this regard, the substitutional atoms can adjust the valence of elements; the degree of regulation is Ni$_2$B < FeNiB < CoNiB for nickel atoms. After the durability test (Fig. 4e), both Ni–B and Ni^0 peaks disappear and Ni 2p of all three samples shift to a higher binding energy in comparison with the initial state. This phenomenon may be related to the formation of active intermediates. Interestingly, the binding energy deviations of CoNiB and FeNiB for Ni 2p are different, following the trend of Ni$_2$B > FeNiB > CoNiB. During the electrochemical process, for Ni$_2$B, nickel is the only catalytic element, so the valency of nickel atoms is increased due to the oxidation effect at the anode to obtain higher efficiency of binding the OER intermediate.

Cobalt and iron atoms in CoNiB and FeNiB are first oxidized due to their weaker electrontivity in comparison with nickel. Cobalt/iron as a major absorber of OH$^-$ keeps nickel from being overoxidized. Thus, the binding energy of nickel is the lowest one in the three synthesized samples. The LSV curves illustrate that the Fe doping effectively enhances the OER properties of FeNiB, which proves the essential role of iron in catalysis and then protects the nickel from being further oxidized. Besides, the intensity ratio of TM–O peaks to TM–B peaks of Fe/Co/Ni from XPS results of the as-prepared samples also supports the oxidation order of Fe/Co/Ni. The Ni 2p spectra of Ni$_2$B, CoNiB and FeNiB indicate that the introduction of Fe and Co atoms adjusts the binding energy of Ni atoms to form appropriate convert acceptor sites. In this respect, the homogeneous heteroatom substitution is conducive to obtaining the structure closer to the adsorption energy volcano top.

X-ray absorption spectroscopy (XAS) is performed to comprehend the electronic interaction of different metal elements. The K-edge X-ray Absorption Near Edge Spectra (XANES) of Fe/Co/Ni can be used to detect the changes of 3d orbital electrons, so the K-edge absorption spectra for all metals are collected and shown in Fig. 5a and S13.†[36] Compared with nickel foil, the weaker normalized absorption intensity of Ni$_2$B, CoNiB, and FeNiB at a lower energy (red rectangle) indicates that the energy of X-ray is not sufficient for the electron transfer from 1s to 3d orbitals due to the decreased screening of the nuclear charge, suggesting the electron transfer from metals to borons. The first derivation of XANS is also illustrated in Fig. S13c, d and S14† in order to intuitively probe the high

6472 | *J. Mater. Chem. A*, 2021, **9**, 6469–6475

This journal is © The Royal Society of Chemistry 2021
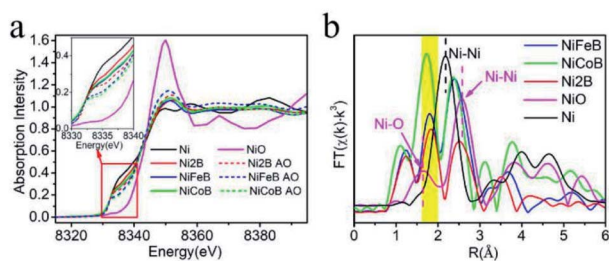
Fig. 5 (a) XANES (X-ray absorption near edge spectra) of nickel contained compounds before and after the OER collected at the Ni K-edge (AO means after the OER). (b) Fourier transformed k^3 weighted EXAFS oscillations measured at the Ni K-edge.

energy shifts of the absorption-edge which represent the increase of valence;[37,38] CoNiB and Co_2B show a slight diversity for the K absorption edge, but a slightly higher energy shift of CoNiB can be found, and the scenario is similar to that of FeNiB and Fe_2B. The increased intensities of absorption-edges from the first derivative curves and slightly high-energy shifts of the absorption-edge of NiCoB and NiFeB are observed in Fig. S14,† suggesting the increased binding energy of nickel. The results related to binding energy are consistent with the XPS analysis. After the OER process, the intensity of all pre-edges decreases, which indicates that the average valences of nickel in these compounds increase during the electrochemical process.[39] However, the short-range structure around the absorption center (Ni) may remain unchanged during the OER, because the oscillation trend of post edges has no evident changes, which supports that the dominated substance is well maintained. The produced nickel oxides/(oxy)hydroxides account for the diversity of XANES spectra, agreeing with the results of XPS.[40–43] The peaks (in the yellow shadow) shown in Fig. 5b represent the TM–B bonds in different compounds (the first element in the chemical formula is the absorption center). The peaks of Ni–B bonds from the three compounds are very close to each other, agreeing well with the similar bond lengths. The Ni–O bonds from the reference sample are shorter than the TM–B bonds. Low-R shifts are found in CoNiB and FeNiB compared with Ni_2B due to the different degree of surface oxidation of the as-prepared fine particles. The Fourier transformed $k3$ weighted EXAFS (extended X-ray absorbtion fine structure) oscillations of the Ni/Fe K edge from FeNiB and the Ni/Co K edge from CoNiB are also compared in Fig. S15;† it is found that the peaks from FeNiB (Fe K edge) and CoNiB (Co K edge) in the yellow shadow have low-R shifts compared to those of the Ni K edge in FeNiB and CoNiB, which is probably caused by the higher oxidation degree of Co and Fe on the sample surface, so that the low-R shifts of the first peaks are affected by the Fe–O or Co–O bonds with shorter bond lengths.

As shown in TEM images (Fig. 6a and b), there is an obvious oxidation layer on the surface of FeNiB after the 30 h OER durability test. HRTEM images (Fig. 6c) of the surface layer exhibit a disordered nano-crystalline distribution. In order to verify the phase of these nanocrystals, we measured their lattice parameters of about 0.272 nm, which corresponds to the (100)
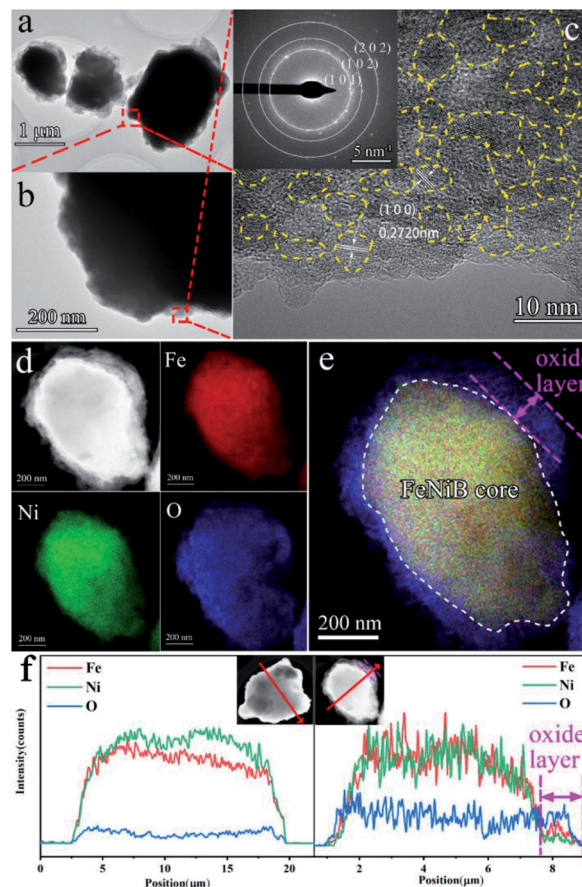
Fig. 6 TEM results of FeNiB after the durability test (a) and (b); (c) TEM image under different magnifications, (d) HRETM image and the SAED image (inset), (e) EDS mapping and (f) EDS line scanning result before and after the durability test.

facet of $Ni (OH)_2$ (0.2707 nm). The SAED results also show the polycrystalline diffraction rings along with a wide amorphous wide band, consistent with HRTEM results. As Fig. 6c shows, most of these nano-polycystallized $Ni(OH)_2$ are below 10 nm in size. Moreover, there are grain boundaries, residual stress and surface defects, which might greatly promote its catalytic activity.[44] EDS mapping results (Fig. 6d and e) exhibit a homogeneous distribution of Fe and Ni elements. The EDS line scanning of a single FeNiB particle before and after the durability test (Fig. 6f) further proves the formation of active oxygen intermediates during the surface reconstruction process. The enhancement of the characteristic peak of the O element means the formation of active oxidation sites such as Fe/Ni oxides and hydroxides.

To further understand the mechanism of Ni–Fe interactions and its effect on the electrocatalytic performance, DFT calculations are performed for binary Ni_2B, Fe_2B and ternary FeNiB structures. The density of states of all three structures are obtained and the d-band center of Fe and the Ni PDOS are calculated (Fig. S16†). It can be seen that the significant overlap arising from 3d states between Ni and Fe atoms and some slight prominent peaks near the Fermi energy are expected to improve adsorption properties and reactivity. Fig. 7 shows the spin-down

This journal is © The Royal Society of Chemistry 2021

J. Mater. Chem. A, 2021, 9, 6469–6475 | 6473
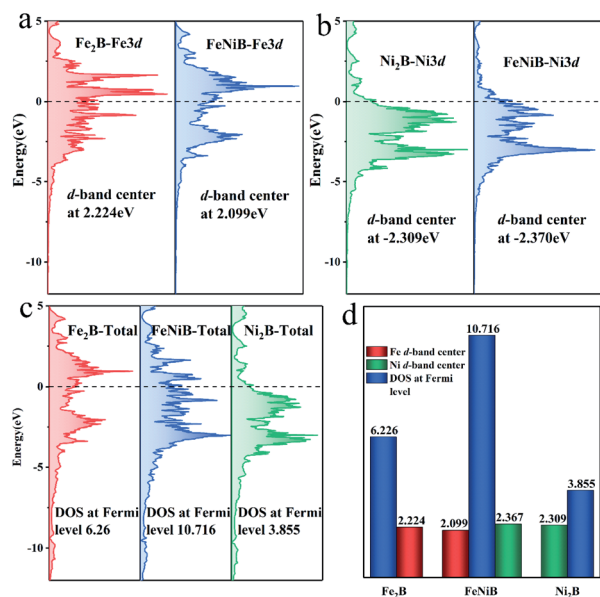
Fig. 7 Spin down orbital (a) Fe-3d PDOSs of Fe$_2$B and FeNiB; (b) Ni-3d PDOSs of Ni$_2$B and FeNiB; (c) Total DOSs of Fe$_2$B, FeNiB and Ni$_2$B; (d) the summary of the d-band center and DOS at the Fermi level.

DOS of the Fe-3d orbitals of Fe$_2$B and FeNiB, Ni-3d orbitals of Ni$_2$B and FeNiB, and the total DOS, respectively. As shown in Fig. 7d, the d-band center of Ni in FeNiB is just slightly higher than that of Ni$_2$B (0.058 eV), and the d-band center of Fe is obviously lower than that of Fe$_2$B (0.125 eV). The d-band center of Fe in FeNiB is much higher than that of Ni, suggesting that Fe can integrate with oxygen more easily. According to d-band center theory, the electrocatalysts with the d-band center close to the Fermi level usually exhibit better electrochemical catalytic performance owing to the moderate absorption and desorption effect toward the intermediate products.[45] Moreover, according to the Boltzmann equation, the electroconductivity is proportional to the DOS near the Fermi level.[46] The DOS near the Fermi level of FeNiB is 10.72, which is 1.72 times higher than that of Fe$_2$B (6.23) and 2.78 times higher than that of Ni$_2$B (3.86). This indicates that the enhanced electroconductivity of FeNiB is due to Ni and Fe atom interactions, which is also consistent with the EIS result during the OER process.

Conclusions

In summary, we have synthesized Fe/Co doped Ni$_2$B catalysts *via* a high pressure and high temperature method. The results show that all samples obtained here are a highly crystalline single phase, and the substituted atoms are uniformly distributed in the lattice. We also found that the FeNiB catalyst stands out for the OER and overall water splitting and is much better than commercial benchmark RuO$_2$. FeNiB could also maintain high electrocatalytic activity at large current density with long-term stability under alkaline conditions. Interestingly, FeNiB exhibits the smallest electrochemical surface area (ECSA), but the highest number of efficient active sites as proved by the TOF test. The XRD, XPS and XANES results illustrate that the non-

linear change of structural parameters by doping with cobalt and iron has dramatic influence on the valence of metal and the electronic structure in this system. And thus the surface oxidation of as-prepared FeNiB increased unusually, which further promoted the dissolution of boron oxides and expose of more Fe/Ni active sites. DFT calculations based results suggested that FeNiB obtained a Ni d-band center similar to that of Ni$_2$B and a Fe d-band center closer to the Fermi level than that of Fe$_2$B. This work provides a new insight into the design of effective electrocatalysts and the effect of doping on oxygen evolution activity.

Conflicts of interest

There are no conflicts to declare.

Acknowledgements

References

1 S. Gupta, M. K. Patel, A. Miotello and N. Patel, *Adv. Funct. Mater.*, 2020, **30**, 1906481.
2 A. Grimaud, A. Demortière, M. Saubanère, W. Dachraoui, M. Duchamp, M.-L. Doublet and J.-M. Tarascon, *Nat. Energy*, 2016, **2**, 16189.
3 N. Danilovic, R. Subbaraman, K. C. Chang, S. H. Chang, Y. Kang, J. Snyder, A. P. Paulikas, D. Strmcnik, Y. T. Kim, D. Myers, V. R. Stamenkovic and N. M. Markovic, *Angew. Chem., Int. Ed.*, 2014, **53**, 14016–14021.
4 S. Laha, Y. Lee, F. Podjaski, D. Weber, V. Duppel, L. M. Schoop, F. Pielnhofer, C. Scheurer, K. Müller, U. Starke, K. Reuter and B. V. Lotsch, *Adv. Energy Mater.*, 2019, **9**, 1803795.
5 X. Li, H. Liu, Z. Chen, Q. Wu, Z. Yu, M. Yang, X. Wang, Z. Cheng, Z. Fu and Y. Lu, *Nat. Commun.*, 2019, **10**, 1409.
6 X. Zhang, Y. Zhao, Y. Zhao, R. Shi, G. I. Waterhouse and T. Zhang, *Adv. Energy Mater.*, 2019, **9**, 1900881.
7 M. Jiang, J. Li, J. Li, Y. Zhao, L. Pan, Q. Cao, D. Wang and Y. Du, *Nanoscale*, 2019, **11**, 9654–9660.
8 H. Zhang, W. Zhou, J. Dong, X. F. Lu and X. W. Lou, *Energy Environ. Sci.*, 2019, **12**, 3348–3355.
9 W. Peng, J. Li, K. Shen, L. Zheng, H. Tang, Y. Gong, J. Zhou, N. Chen, S. Zhao, M. Chen, F. Gao and H. Gou, *J. Mater. Chem. A*, 2020, **8**, 23580–23589.
10 Y. Guo, T. Park, J. W. Yi, J. Henzie, J. Kim, Z. Wang, B. Jiang, Y. Bando, Y. Sugahara, J. Tang and Y. Yamauchi, *Adv. Mater.*, 2019, **31**, 1807134.
11 X. Zheng, X. Han, Y. Zhang, J. Wang, C. Zhong, Y. Deng and W. Hu, *Nanoscale*, 2019, **11**, 5646–5654.

12 J. Wang, T. Ouyang, N. Li, T. Ma and Z. Liu, *Sci. Bull.*, 2018, **63**, 1130–1140.

13 X. Jia, Y. Zhao, G. Chen, L. Shang, R. Shi, X. Kang, G. I. Waterhouse, L. Wu, C. Tung and T. Zhang, *Adv. Energy Mater.*, 2016, **6**, 1502585.

14 S. Wang, P. He, Z. Xie, L. Jia, M. He, X. Zhang, F. Dong, H. Liu, Y. Zhang and C. Li, *Electrochim. Acta*, 2019, **296**, 644–652.

15 X. Chen, Z. Yu, L. Wei, Z. Zhou, S. Zhai, J. Chen, Y. Wang, Q. Huang, H. E. Karahan, X. Liao and Y. Chen, *J. Mater. Chem. A*, 2019, **7**, 764–774.

16 Z. Shi, H. Yin, Z. Xu, T. Zhang, G. Yang, Q. Zheng, R. S. Rao, J. Yang, F. Gao, M. Wu and X. Qu, *Intermetallics*, 2019, **114**, 106573.

17 A. Benamor, S. Kota, N. Chiker, A. Haddad, Y. Hadji, V. Natu, S. Abdi, M. Yahi, M. E. A. Benamar, T. Sahraoui, M. Hadji and M. W. Barsoum, *J. Eur. Ceram. Soc.*, 2019, **39**, 868–877.

18 Z. Zhang, G. Yao, L. Zhang, P. Jia, X. Fu, W. Cui and Q. Wang, *J. Magn. Magn. Mater.*, 2019, **484**, 154–158.

19 H. Tang, X. Gao, J. Zhang, B. Gao, W. Zhou, B. Yan, X. Li, Q. Zhang, S. Peng, D. Huang, L. Zhang, X. Yuan, B. Wan, C. Peng, L. Wu, D. Zhang, H. Liu, L. Gu, F. Gao, T. Irifune, R. Ahuja, H. K. Mao and H. Gou, *Chem. Mater.*, 2020, **32**, 459–467.

20 H. Gou, N. Dubrovinskaia, E. Bykova, A. A. Tsirlin, D. Kasinathan, W. Schnelle, A. Richter, M. Merlini, M. Hanfland, A. M. Abakumov, D. Batuk, G. Van Tendeloo, Y. Nakajima, A. N. Kolmogorov and L. Dubrovinsky, *Phys. Rev. Lett.*, 2013, **111**, 157002.

21 H. Yuan, S. Wang, X. Gu, B. Tang, J. Li and X. Wang, *J. Mater. Chem. A*, 2019, **7**, 19554–19564.

22 Y. Li, B. Huang, Y. Sun, M. Luo, Y. Yang, Y. Qin, L. Wang, C. Li, F. Lv, W. Zhang and S. Guo, *Small*, 2019, **15**, 1804212.

23 N. Xu, G. Cao, Z. Chen, Q. Kang, H. Dai and P. Wang, *J. Mater. Chem. A*, 2017, **5**, 12379–12384.

24 J. Zhang, X. Li, Y. Liu, Z. Zeng, X. Cheng, Y. Wang, W. Tu and M. Pan, *Nanoscale*, 2018, **10**, 11997–12002.

25 H. Mao, X. Guo, Y. Fu, H. Yang, Y. Zhang, R. Zhang and X. Song, *J. Mater. Chem. A*, 2020, **8**, 1821–1828.

26 J. Masa, P. Weide, D. Peeters, I. Sinev, W. Xia, Z. Sun, C. Somsen, M. Muhler and W. Schuhmann, *Adv. Energy Mater.*, 2016, **6**, 1502313.

27 J. Masa, I. Sinev, H. Mistry, E. Ventosa, M. de la Mata, J. Arbiol, M. Muhler, B. R. Cuenya and W. Schuhmann, *Adv. Energy Mater.*, 2017, **7**, 1700381.

28 N. Xu, G. Cao, Z. Chen, Q. Kang, H. Dai and P. Wang, *J. Mater. Chem. A*, 2017, **5**, 12379.

29 C. C. L. McCrory, S. Jung, I. M. Ferrer, S. M. Chatman, J. C. Peters and T. F. Jaramillo, *J. Am. Chem. Soc.*, 2015, **137**, 4347–4357.

30 W. Yuan, X. Zhao, W. Hao, J. Li, L. Wang, X. Ma and Y. Guo, *ChemElectroChem*, 2019, **6**, 764–770.

31 J. M. V. Nsanzimana, Y. Peng, Y. Y. Xu, L. Thia, C. Wang, B. Y. Xia and X. Wang, *Adv. Energy Mater.*, 2018, **8**, 1701475.

32 F. Guo, Y. Wu, H. Chen, Y. Liu, L. Yang, X. Ai and X. Zou, *Energy Environ. Sci.*, 2019, **12**, 684–692.

33 C. Wang, H. Daimon, T. Onodera, T. Koda and S. Sun, *Angew. Chem., Int. Ed.*, 2008, **120**, 3644–3647.

34 A. S. Hesham and P. R. Watson, *Appl. Surf. Sci.*, 1997, **108**, 371–377.

35 M. C. Biesinger, B. P. Payne, A. P. Grosvenor, L. W. M. Lau, A. R. Gerson and R. S. C. Smart, *Appl. Surf. Sci.*, 2011, **257**, 2717–2730.

36 K. Huang, R. Wang, S. Zhao, P. Du, H. Wang, H. Wei, Y. Long, B. Deng, M. Lei, B. Ge, H. Gou, R. Zhang and H. Wu, *Energy Storage Materials*, 2020, **29**, 156–162.

37 S. Xu, M. Wang, G. Saranya, N. Chen, L. Zhang, Y. He, L. Wu, Y. Gong, Z. Yao, G. Wang, Z. Wang, S. Zhao, H. Tang, M. Chen and H. Gou, *Appl. Catal., B*, 2020, **268**, 118385.

38 S. Xu, X. Gao, A. Deshmukh, J. Zhou, N. Chen, W. Peng, Y. Gong, Z. Yao, K. D. Finkelstein, B. Wan, F. Gao, M. Wang, M. Chen and H. Gou, *J. Mater. Chem. A*, 2020, **8**, 2001–2007.

39 Y. Xie, J. Cai, Y. Wu, Y. Zang, X. Zheng, J. Ye, P. Cui, S. Niu, Y. Liu, J. Zhu, X. Liu, G. Wang and Y. Qian, *Adv. Mater.*, 2019, **31**, 1807780.

40 P. W. Menezes, A. Indra, I. Zaharieva, C. Walter, S. Loos, S. Hoffmann, R. Schlögl, H. Dau and M. Driess, *Energy Environ. Sci.*, 2019, **12**, 988–999.

41 P. Zhang, X. F. Lu, J. Nai, S. Q. Zang and X. W. Lou, *Adv. Sci.*, 2019, **6**, 1900576.

42 L. An, J. Feng, Y. Zhang, R. Wang, H. Liu, G. C. Wang, F. Cheng and P. Xi, *Adv. Funct. Mater.*, 2019, **29**, 1805298.

43 B. Ravel and M. Newville, *J. Synchrotron Radiat.*, 2005, **12**, 537–541.

44 L. Wang, J. Li, X. Zhao, W. Hao, X. Ma, S. Li and Y. Guo, *Adv. Mater. Interfaces*, 2019, **6**, 1801690.

45 A. Wang, Z. Zhao, D. Hu, J. Niu, M. Zhang, K. Yan and G. Lu, *Nanoscale*, 2019, **11**, 426.

46 P. C. Wei, C. X. Cai, C. R. Hsing, C. M. Wei, S. H. Yu, H. J. Wu, C. L. Chen, D. H. Wei, D. L. Nguyen, M. M. C. Chou and Y. Y. Chen, *Sci. Rep.*, 2019, **9**, 8616.

This journal is © The Royal Society of Chemistry 2021

J. Mater. Chem. A, 2021, **9**, 6469–6475 | **6475**